LUND UNIVERSITY
Faculty of Science

Photoconductivity in functionalized oxide films

Aitor De Andres Gonzalez

Thesis submitted for the degree of Master of Science
Project duration : 5 months
Supervised by H.G.Svavarsson and I. Maximov

Department of physics
Division of solid state physics
January 2018

In collaboration with

HÁSKÓLINN Í REYKJAVÍK
REYKJAVIK UNIVERSITY

Contents

1 Introduction **6**

2 Theoretical background **8**

2.1 Photoconductivity in semiconductors bulk . . . 8

2.1.1 Optical absorption . . . 8

2.1.2 Electrical conductivity . . . 10

2.2 Photoconductivity in low dimensional structures . . . 12

3 Materials and method **15**

3.1 Instrumentation . . . 15

3.2 Experimental strategy . . . 17

3.3 Magnetron sputtering . . . 17

3.4 X-ray characterization methods . . . 18

3.4.1 X-ray reflectometry (XRR) . . . 19

3.4.2 Grazing Incidence X-Ray Diffraction (GiXRD) . . . 21

4 Results and discussion **23**

5 Outlook **36**

Bibliography **37**

List of acronyms

Acronym	Meaning
AFM	atomic force microscope
DC	direct current
GiXRD	grazing incidence X-ray diffraction
MS	magnetron sputtering
QD	quantum dot
QW	quantum well
RF	radio frequency
TEM	transmission electron microscope
UV	ultraviolet
XRR	X-ray reflectivity

Abstract

Light matter interaction in low dimensional structures is a rich field of study involved in both fundamental and applied research. However, the accurate and scalable processing of nanostructures required to produce the desired low dimensional devices still remains a challenge in many cases. This thesis explored the sample processing for the scalable production of photoconductive films with high spectral sensitivity. The samples consisted in several thin layers ($\leq$ 100 nm) of SiO_2 and SiGe, which were deposited using magnetron sputtering. The samples were processed against different deposition and annealing temperatures and using silicon monocrystal (001) and borosilicate glass as substrates. Their structure and photoconductive properties were characterized using X-ray reflectivity (XRR), grazing incidence X-ray diffraction (GiXRD), atomic force microscope (AFM), optical microscope and optoelectrical measurements. The results show higher degree of crystallization and better photoconductive properties for the samples deposited on hot substrate (300-700°C), rather than those deposited at room temperature and annealed afterwards. In particular, one sample with spectrum-selective photoconductive properties was achieved. Besides that, the SiGe aggregation phenomenon was observed through AFM, showing the formation of relatively homogeneous clusters, which are thought to be precursors in the nanocrystals formation.

Acknowledgements

H.G.Svavarsson

I.Maximov

M.T.Sultan

A.G.Lopez

V.D.A.Arrola

This thesis was a lot of fun and a great personal and academic experience, but it would not have been possible without the help of several people. First of all, I would like to thank my supervisor, Halldor Guðfinnur Svavarsson from Reykjavik University, for being so kind and doing his best to pave my way towards my goals. His advice and guidance was a gamechanger through my research experience in Iceland. Secondly, I want to acklowledge Muhamad Taha Sultan, for his infinite pacience towards my never ending questions, problems and crazy ideas. Third, I want to thank Ivan Maximov, for being so flexible with this project even before it started. Next, I would like to thank my parents, Asun Gonzalez Lopez and Victor De Andres Arrola, because without their constant and strong support my university studies might not had started in the first place. And finally, I would like to thank all the people from Iceland University who was always there to solve my questions, provide ideas and look after my unexperienced interaction with the experimental equipment.

Chapter 1

Introduction

During the last decades, the boosted expansion of semiconductor technology has opened an endless amount of opportunities for both science and industry. As processed structures shrinked into the nanometer range, it became possible to directly observe and control several quantum mechanical effects, until then hidden in the average properties of materials bulk. Among them, the quantum confinement effect in low dimensional structures is perhaps one of the most mindblowing, and the new physics that came with it constitute a game changer in several fields of science. However, the accurate and reproducible processing of nanostructures is still an open challenge, and many existing methods are of difficult scalability and implementation in industry.

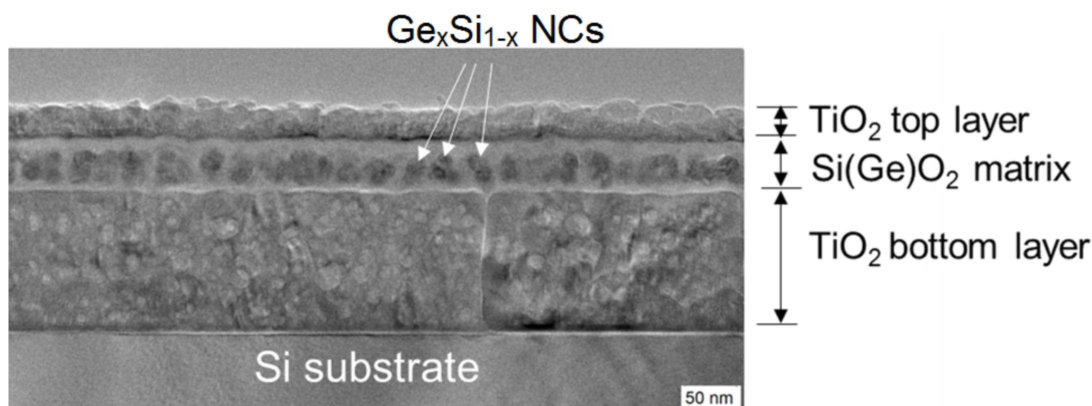

Figure 1.1: TEM image of SiGe/TiO_2 cross section, extracted from [1] with their permission.

In this thesis, the possibility of using low dimensional structures for highly selective light detection has been explored experimentally. To that end, thin layers of silicon-germanium (SiGe) and silicon oxide (SiO_2) were deposited in the lab using different sputtering methods. Upon annealing, the SiGe layers are expected to aggregate forming nanocrystals inside a matrix of oxide. Due to quantum confinement [2], such structure is thought to show highly selective photoconductivity. These assumptions build up on the results recently achieved by [1], where they managed to process a similar sample using SiGe and TiO_2, as it can be seen in the transmission electron microscope (TEM) image in figure 1.1. The nanocrystals were achieved after deposition and annealing cycles at different temperatures. Slav et al. demonstrated that such structure is photoconductive under illumination of ultraviolet (UV) light, possibly due to the intrinsec properties of TiO_2 in the oxide layers. However, they did not achieve the desired functionability in

the infrared range of the spectrum. In this thesis, the motivation for using SiO_2 relies on its dielectric properties and its ubiquitous industrial implementation. Because of its high band gap value, SiO_2 is expected to behave as a passive layer in the near ultraviolet range, allowing this study to focus on the nanocrystals as the only active structure. Other relevant state-of-art studies include the work done by [3] where tunneling transport through germanium nanocrystals in SiO_2 matrix was studied, or by [4] who produced strained SiGe quantum wells (QW) that were used for achieving large quantum coherence gain.

The physical principle behind the selective photoconductivity consists on trapping the photogenerated electrical carriers in well defined states of the nanocrystals; these behave as potential wells where quantum confinement applies in all three physical dimensions and approach the zero dimensional behavior of quantum dots (QDs) [2]. Under applied bias, the electron-hole pairs are able to tunnel through the SiO_2 matrix and to create neat charge flow, as symbolically sketch in figure 1.2. To control the wavelengths of resonant absorption, the experimental processing conditions for the growth of nanocrystals with the desired sizes are investigated and optimized in this study. A theoretical background for the basic understanding of the expected phenomena, processing and characterization methods is included. However, an advanced theoretical modeling of the photoconductive phenomenon is beyond the scope of this thesis.

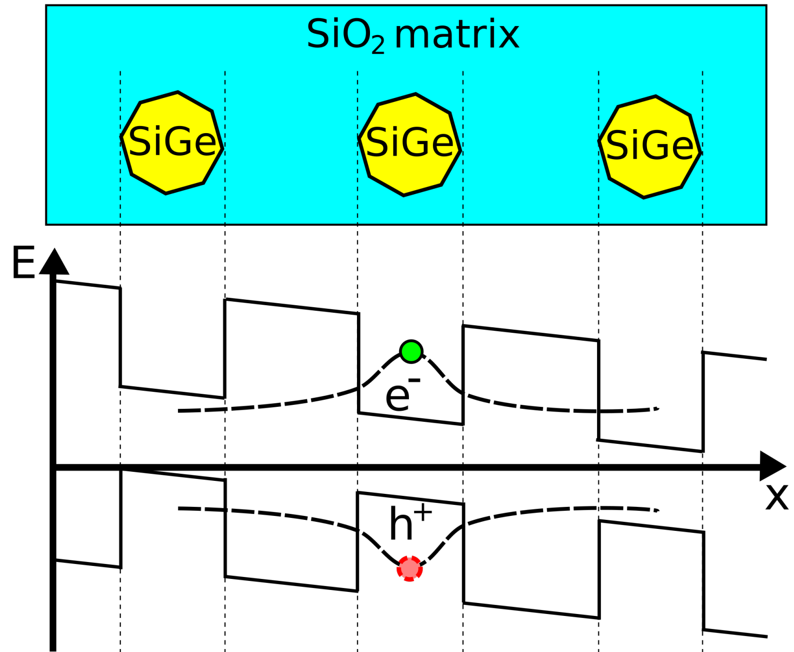

Figure 1.2: Energy band diagram across SiGe nanocrystals (yellow octagons) behaving as quantum wells (QW). The wells are oblique due to the constant potential gradient, which is created by the applied electrical bias.

The outcome of this thesis is expected to positively contribute into the knowledge of the experimental processing of nanocrystals and thin films. Due to the widespread implementation of silicon and germanium in the semiconductor industry, and also to the simplicity and scalability of the chosen processing methods, the possible applications that might derive from the developed photoconductive layers are many and diverse. Optoelectrical devices for environmental sensing, food safety and biomedical monitoring are only some examples. In particular, the highly selective photoconductive response might be useful for applications that require identification between similar spectra. As an example, identification between the reflection spectrum of icy, wet and dry asphalt could lead to a major advance in road security.

Chapter 2

Theoretical background

The following chapter is a quick theoretical review of some topics that the author considered critical for the proper understanding of the experimental part. While a very simplified approach has been adopted whenever possible, references to recommended literature have been included in every section for a deeper and more detailed description.

2.1 Photoconductivity in semiconductors bulk

Photoconductivity is the change of the electrical conductivity in a material upon interaction with incident electromagnetic radiation. This phenomenon can manifest itself either by an increased electrical conductivity (known as positive photoconductivity) or by a decreased one (i.e. negative photoconductivity), even though the physical mechanisms underneath them might be different.

2.1.1 Optical absorption

In general, the absorption of optical radiation[1] in a semiconductor takes place through the photoeffect [5], where electrons are excited from their inital state into states of higher energy [5]. The photoeffect can either be external[2] or internal, depending on whether the final state is the vacuum level (i.e. a free particle) or a bound state in the lattice band structure, respectively. In the frame of photoconductivity, the *internal* photoeffect is the relevant phenomenon to deepen in.

In undoped semiconductors at any non-zero temperature, electrons tend to occupy states in the valence band while the conduction band remains almost empty[3]. As photons with energy $E_{ph} = \hbar\omega_{ph}$ are irradiated and propagate through the crystal, they can be absorbed and induce interband transitions. Every absorption event produces one electron-hole pair, whose components survive independently for a certain time before the recombination takes place. The probability that a photon is absorbed in the crystal is defined as the quantum efficiency and denoted as η, and the mean time between the absorption and the recombination as τ_r. If the photon flux is high enough, a significant

[1] The optical range of the electromagnetic spectrum is conventionally defined between 100 nm and 1 mm in wavelength.

[2] Commonly known as photoemission or as photoelectric effect, where electrons are ejected as free particles.

[3] For $T > 0$ K, the tail of the Fermi distribution predicts thermal excitation for a fraction of the statistical population.

amount of the valence band electrons may be transferred into the conduction band, giving rise to the electronic population inversion [6]. For a single event, energy conservation demands that the absorption may occur only if

$$E_{ph} \geq E'_g \tag{2.1}$$

where E'_g is the minimum energy difference between the bands. The fact that the states in the conduction band are well defined into the reciprocal space still imposes further selection rules due to momentum conservation[4]:

$$\hbar\Delta\mathbf{k} = \hbar\mathbf{k_{ph}} \tag{2.2}$$

where $\mathbf{k}$ and $\mathbf{k_p h}$ are the crystal and photon wave vectors, respectively.

Semiconductor materials can be classified into direct or indirect, depending whether the highest maximum of the valence band has or not the same momentum as the lowest minimum of the conduction band in the reciprocal space, as can be seen in figure 2.1a.

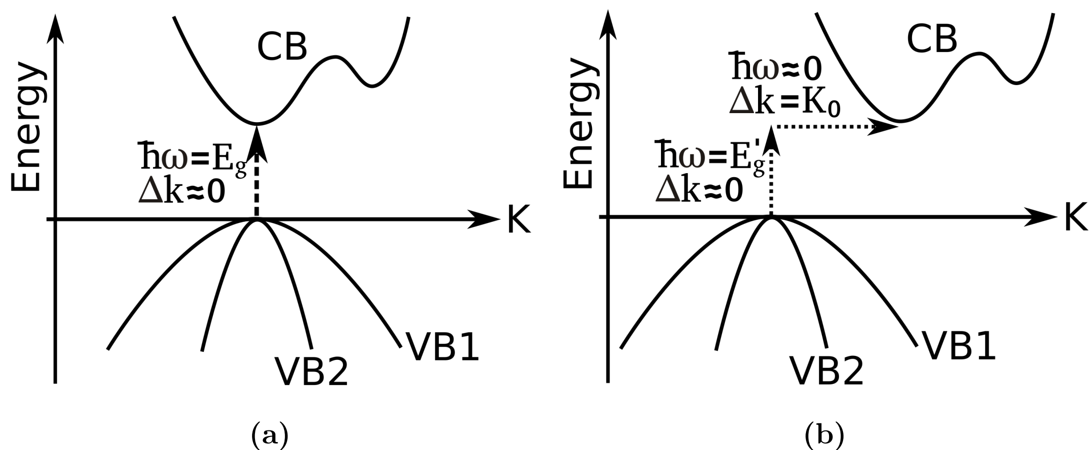

Figure 2.1: Schematic representation of an interband transition in **(a)** direct and **(b)** indirect semiconductors.

While of almost no effect for direct gap semiconductors, where little momentum exchange is involved, equation 2.2 has important consequences when dealing with indirect gaps. The momentum of electrons in the conduction band is approximately of h/R, where R is the interatomic separation in real space, and transitions through indirect gaps are expected to exchange crystal momentum of that same order of magnitude. This is no match for the momentum of an optical photon h/λ, which is much smaller. Therefore, an optical absorption in an indirect band gap semiconductor can only take place if mediated through the lattice phonons, which have little energy (∼meV) but can carry high momentum. Due to the broad distribution of phonon momentum, the onset of optical absorption given by equation 2.1 is much sharper in semiconductors with direct band gap, than in the indirect ones. However even in direct semiconductors, condition 2.1 might in practice be relaxed due to the presence of impurities or coupled states (such as excitons), which add possible states in the absorption spectrum. A final remark about silicon and germanium: even though they are both indirect band gap semiconductors, the $\mathbf{k}$ mismatch for the

[4]This condition is apparently absent in the external photoeffect, where the momentum of the ejected electrons is not restricted to specific values by the lattice.

interband transition of the later one is very small, allowing it to behave similarly as a direct semiconductor under certain conditions.

2.1.2 Electrical conductivity

The conductivity of any sample, stated as σ, is a relation between the current density $\mathbf{j}$ and the applied field $\mathbf{E}$, defined as

$$\mathbf{j} = \sigma \mathbf{E} \tag{2.3}$$

In order to understand how the absorbed light can affect the conductivity, first we must work out the mechanism of charge transport in the lattice. If an external electric field is applied to the semiconductor, the available charge carriers will response by moving through the periodic potential of the lattice. In a classical formalism[5], their movement can be described by

$$m_e \left(\frac{d\mathbf{v_e}}{dt} + \frac{\mathbf{v_e}}{\tau} \right) = -e\mathbf{E} - e\mathbf{v_e} \times \mathbf{B} \tag{2.4}$$

$$m_h \left(\frac{d\mathbf{v_h}}{dt} + \frac{\mathbf{v_h}}{\tau} \right) = +e\mathbf{E} + e\mathbf{v_h} \times \mathbf{B} \tag{2.5}$$

where $\mathbf{E}$ and $\mathbf{B}$ are respectively the electric and magnetic component of the applied field, $m_{e,h}$ the effective mass of electrons and holes, and $\mathbf{v_{e,h}}$ their thermal velocity. The previous equations follow from the Lorentz force with the addition of the term τ, which accounts for the random collisions with the lattice ions or impurities. For a direct current field (DC) field, solving equations (2.4) and (2.5) result in a steady state solution, where the mean velocity and the electric field appear to be proportional:

$$\mathbf{v_e} = -\frac{e\tau}{m_e}\mathbf{E} \tag{2.6}$$

$$\mathbf{v_h} = +\frac{e\tau}{m_h}\mathbf{E} \tag{2.7}$$

The proportionality constant is defined as the carrier mobility, stated as $\mu_{e,h}$. In an intrinsec semiconductor (that is, $n_e = n_h$), it follows immediately that

$$\mu_{e,h} = \frac{e\tau}{m_{e,h}} \tag{2.8}$$

In our classical picture, the electric current density parallel to the applied field is just the amount of charge crossing the section of the crystal per unit time. Using equation 2.3, it leads to:

$$\sigma = e^2\mu \left(\frac{n_e}{m_e} + \frac{n_h}{m_h} \right) = ne(\mu_e + \mu_h) \tag{2.9}$$

The previous expression has already significant importance; it states that the conductivity of the sample depends on both the number of available carriers and their mobilities. When illuminated, the number of carriers in the sample changes as a result of a dynamic process. As explained in the previous section, absorption events populate the sample while

[5] A classical formalism is well suited here because it is possible to prove that a quantum mechanical treatment would give the same equation of motion [6], assuming the wavefunction of the electrons to be much smaller than the size of the crystal in any dimension.

spontaneous recombination events depopulate it. Under a photon flux Φ, the number of carriers changes in time as

$$\frac{dn}{dt} = \eta\Phi - \frac{n}{\tau_r} \tag{2.10}$$

and therefore, we reach that the differential photoconductivity is

$$\frac{d\sigma}{dt} = \frac{d\sigma}{dn}\frac{dn}{dt} = e(\mu_e + \mu_h)\left(\eta\Phi - \frac{n}{\tau_r}\right) \tag{2.11}$$

The reader must notice two facts. Firstly, the previous expression is only valid when the photon flux is low, i.e. when the recombination due to stimulated emission is negligible[6]. Secondly, solving equation 2.11 introduces an integration constant, namely n_{dark}, which has important physical meaning. So far, we have dealt with a number of charge carriers n generated only due to optical absorption, but in practice any crystal contains a number of intrinsic charges, which also contribute to the current. The constant n_{dark} accounts for that intrinsic charge, and the current that generates is called "dark current" in photoconductive experiments.

Finally, there are a couple of cases that are worth solving here, as they will be useful for the experimental analysis. After a while, equation (2.11) leads to a steady state solution. In that case, the number of charges remains constant, and therefore:

$$\eta\Phi = \frac{n}{\tau_r} \tag{2.12}$$

The second case of interest is when the photon flux is suddenly turned off, i.e. $\Phi = 0$. In that situation, integration of the differential photoconductivity becomes straightforward, and the electric current density is:

$$\mathbf{j}(t) = e(\mu_e + \mu_h)\left(n_0 e^{-t/\tau_r} + n_{dark}\right)\mathbf{E} = \left(\sigma_{photo} + \sigma_{int}\right)\mathbf{E} \tag{2.13}$$

where n_0 is the number of existing photogenerated charges (i.e. the total charge minus n_{dark}) when the photon flux is closed, σ_{photo} is the photoconductivity and σ_{int} is the intrinsec conductivity. It is convenient to manipulate the previous expression to make the photoconductivity relative to the intrinsec conductivity. Dividing it by $\mathrm{j_{dark}}$ and doing some basic algebra, the following is reached:

$$\frac{j_{total}}{j_{dark}} - 1 = \frac{\sigma_{photo}}{\sigma_{dark}} \tag{2.14}$$

where the left hand side of the equation is defined as the **normalized photoconductivity**; a dimensionless parameter that expresses the amount of conduction due to photogenerated carriers. In order to give an intuitive idea of the meaning of this concept, the normalized photoconductivity can be calculated in two cases; samples that are not sensitive to light illumination will have normalized photoconductivity of 0, while those where the number of photogenerated charge carriers is the same as the intrinsec charge carriers will have normalized photoconductivity of 1.

[6]As demonstrated in [7], the cross section for excitation and stimulated emission are the same.

2.2 Photoconductivity in low dimensional structures

So far we have approached semiconductor structures assuming them to be an infinite crystalline array. The boundary conditions arising from the borders of the crystal were neglected, and indeed that provides a good framework to understand macroscopic crystals. However, as the structure shrinks into the nanometer size[7], the quantization imposed by crystal boundaries must be taken into account. In order to deal with photoconductivity in low dimensional structures, a quantum formalism must be adopted [2]. If the nanocrystals are assumed to be spherical semiconductor structures within a matrix of insulating oxide, then the system can be modeled as a set of spherical quantum dots (QDs) with square potential. In such model, the band diagram of the system can be approximated using Anderson's rule [2], i.e. aligning the vacuum levels and combining the energy levels of its constituents in the regions of the different materials. The resulting band diagram has been shown in figure 2.2, and predicts the presence of two potential wells within the nanocrystal; one in the conduction band and one in the valence band.

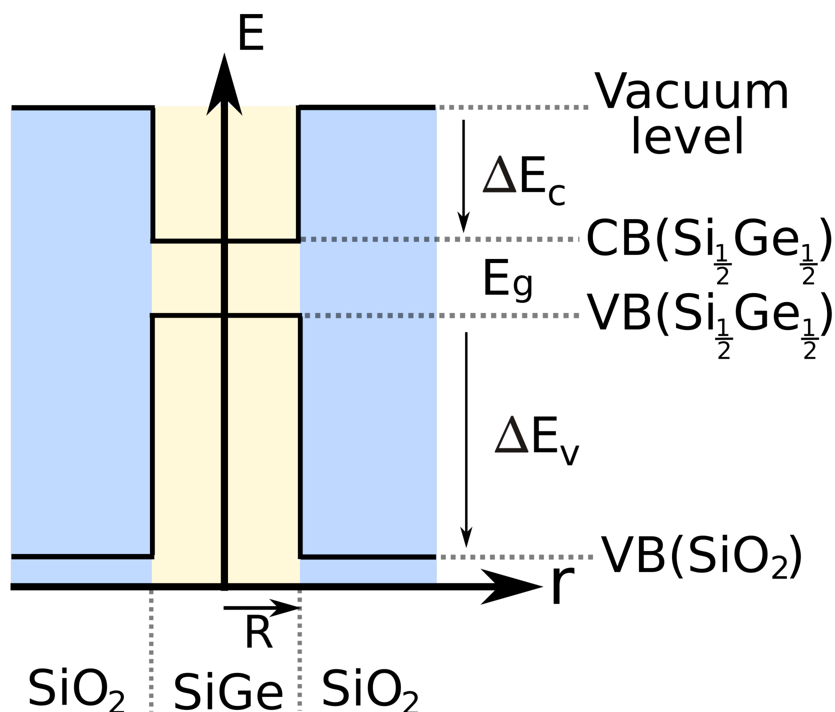

Figure 2.2: Schematic band diagram of a SiGe quantum dot in a matrix of SiO_2.

Electrons can only exist inside the quantum well above the conduction band in specific states with well defined energy, and the same applies for holes below the top of the valence band. Therefore, only photons with energy

$$E_p = E_g + E_e + E_h \tag{2.15}$$

can be absorbed by the nanocrystals, where E_e and E_h are the allowed energies for electrons and holes in the quantum wells of their band, respectively. The allowed energy values inside the wells can be directly measured experimentally in optical absorp-

[7]Rigorously speaking, the quantum confinement must be taken into account when the size of the crystal is comparable to the size of the thermal wave function of the electrons in any direction.

tion experiments[8], or calculated theoretically by solving the time independent Shrödinger equation, which is written in spherical coordinates for convenience as

$$\left\{ \frac{-\hbar^2}{2m}\nabla^2 + V(r) \right\} \psi(r,\theta,\phi) = E\psi(r,\theta,\phi) \tag{2.16}$$

where the potential is

$$V(r) = \begin{cases} \Delta E_{c,v} & \text{if } |r| > R \\ 0 & \text{if } |r| \leq R \end{cases}$$

and where m is the effective mass and $\Delta E_{c,v}$ is the energy difference between either the vacuum level and the conduction band of SiGe, or between the valence bands of SiO_2 and SiGe, as shown in figure 2.2. Due to the potential spherical symmetry, the differential equation (2.16) can be written as a product of two functions with separated variables, i.e. $f(r)f(\theta,\phi)$. The energy of the system in the ground state only depends on the radial function, which can be proven to be

$$-\cot(\gamma) = \sqrt{\frac{mV(2R)^2}{2\hbar^2}\frac{1}{\gamma^2} - 1} \tag{2.17}$$

where the dimensionless parameter $\gamma = kR$ was introduced for convenience, being k the wavenumber of electron and $E = \hbar^2 k^2/2m$ its energy. The solutions of the previous equation were calculated numerically for quantum dots of different sizes, and are plotted in figure 2.3. The reader must realize that the presence of bound states is not granted if the well is too narrow or too shallow. In any case, for the well depth and effective masses imposed by the band structure of $Si_{0.5}Ge_{0.5}$ and SiO_2, the ground state becomes unbound for diameters slightly below 1 nm. Another fact worth mentioning is that equation 2.17 is the same transcendent equation as for a 1 dimensional quantum square well, but considering only its antisymmetric solutions. This arises naturally as the confinement in the QD is isotropic in all directions, but with no symmetric solutions due to the spherical boundary conditions.

Introducing the results of figure 2.3 in equation (2.15) show that resonant absorption could take place for photon energies ranging between two limits. For increasing values of the QD size, the energy of electrons and holes in the ground state decreases rapidly, recovering the photon absorption at $E_{ph} = E_g$ as we approach the macroscopic limit. On the other direction, equation 2.17 predicts that ground states with energies around 1 eV can exist for nanocrystals of 1 nm in diameter. This would imply resonant absorption for $E_{ph} \approx 2$ eV, which already belongs to the visible range and is about twice the band gap of silicon.

[8] In direct gap semiconductors, photoluminescence (PL) experiments are often the most popular choice for measuring E_g, E_e and E_h. However, this approach is of difficult application in indirect gap semiconductors, due to their little emission efficiency.

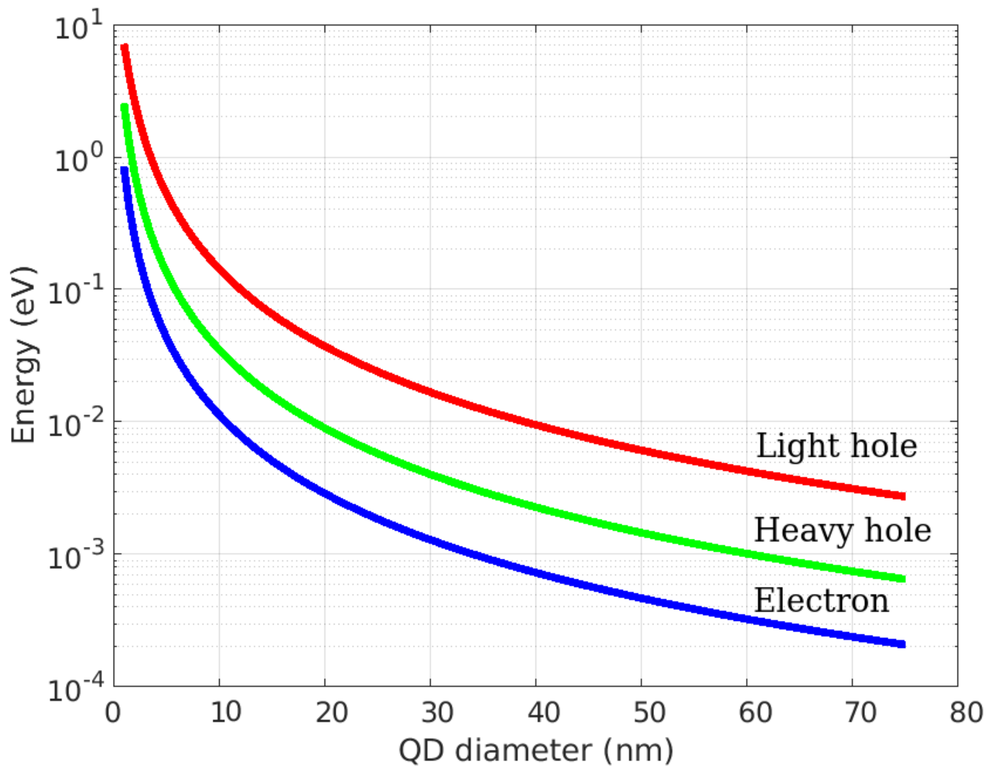

Figure 2.3: Ground state energy in a spherical quantum well as a function of its diameter. The Schrödinger equation was solved numerically for a square potential of 4.07 eV depth for electrons with relative mass of 1.28, and for 10 eV depth for light and heavy holes with relative masses of 0.097 and 0.41, respectively. Values extracted from [2], considering the effective mass of $Si_{0.5}Ge_{0.5}$ to be in the L direction of the reciprocal unit cell.

Chapter 3

Materials and method

3.1 Instrumentation

Wafers of silicon monocrystal (001) and borosilicate glass were used as the sample substrate. Prior to deposition, the substrates were cleaned in three different ultrasonic baths, using acetone, methanol and isopropanol for 4 minutes each. When using borosilicate glass as substrate, the growth of the samples was performed in a vacuum chamber optimized for magnetron sputtering deposition, which was baked for 24 hours at 180 °C before starting the experiments as schematically shown in figure 3.1. The chamber integrates two 3-inch targets of silicon and germanium, with purities of 99.999% in both cases. The targets were connected to DC and RF power supplies for sputtering in the two respective modes as desired, and were water cooled. The temperature of the samples during deposition was controlled using a heater build in the sample holder, which could be set within the range 25 - 700 °C, and was measured with a thermocouple with precision of $\pm 5^oC$ for that range[1]. During deposition, the sample holder was continuously rotated using a motorized arm to even the film growth. The flow of Ar and O_2 mixture into the chamber was adjusted using two mass flow controllers, and the base pressure before introducing the mixture was below $1 \cdot 10^{-8}$ mbar, which was kept by a molecular turbopump. The deposition process could be easily turned on/off by using pneumatic shutters build on the top of every target, which were computer controlled. The deposition rate was calibrated to be of 3.6 nm/min for Ge and 3.45 nm/min for silicon at 25 W and 85 W power in DC mode, respectively. This provides a SiGe ratio of nearly 50% each, at deposition pressure of $7 \cdot 10^{-}3$ mbar. For deposition of SiO_2, 150 W in RF mode were measured to provide 5.3 nm/min, using the Si target in a reactive atmosphere of 4% oxigen at a total pressure of $2.3 \cdot 10^{-3}$ mbar. The sample annealing was performed using rapid thermal annealing (RTA) [8] at pressure of $3 \cdot 10^{-5}$ mbar.

Due to limited availability to access the experimental equipment described above, the sample growth on Si substrate was performed in a different vacuum chamber with base pressure of $5 \cdot 10^{-7}$ mbar, which was kept by a cryopump. The chamber integrated a two inch SiO_2 target with purity of 99.999%, which was sputtered using a RF power supply. A SiGe target was build by carefully assembling pieces of Si and Ge crystal on a two inch Si wafer, giving measured rate of deposition of $Si_{0.4}Ge_{0.6}$, and was sputtered in DC mode. The purity of the assembled target was unknown, but it was of 99.999% for the

[1] Even though the thermocouple had much higher precision, the heat transfer process from the build-in heater until sample required some time to stabilize and reach a nearly-steady temperature, and even then the presence of heat waves arose as small temperature oscillations.

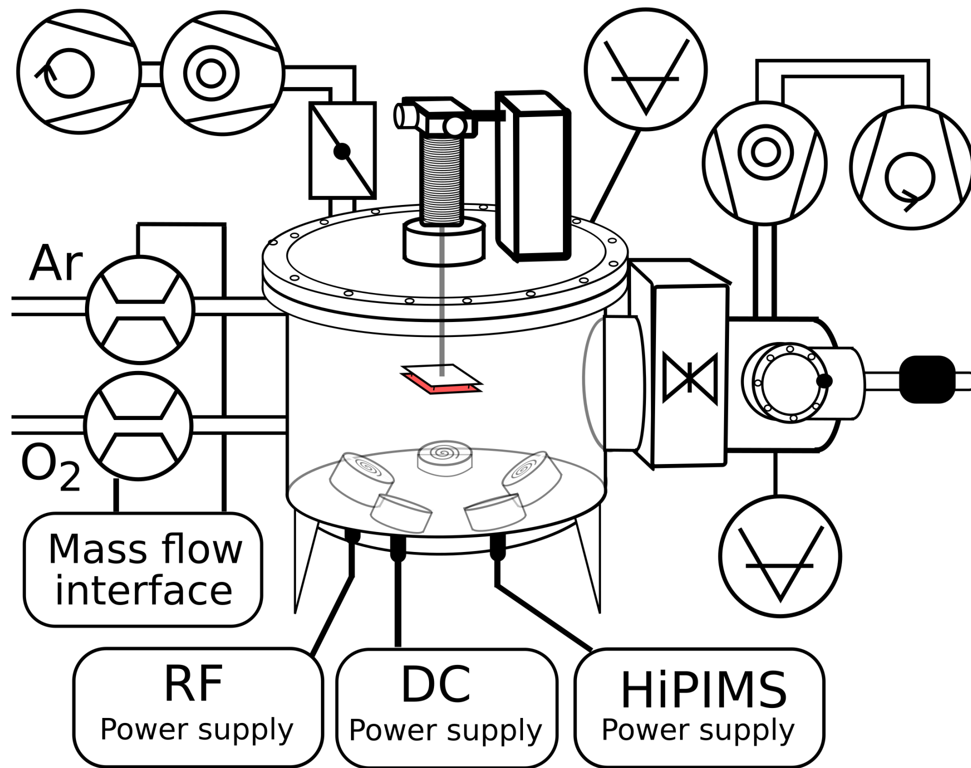

Figure 3.1: Scheme of the sputtering chamber used for the sample processing.

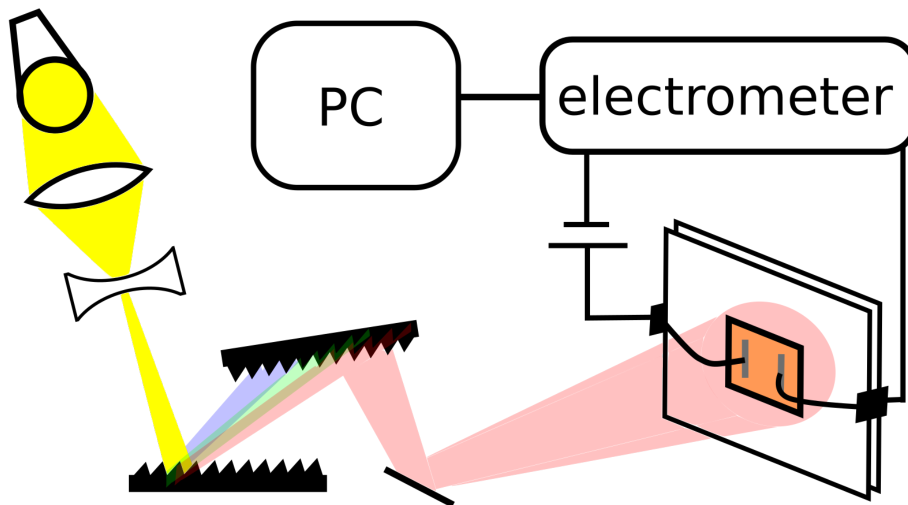

Figure 3.2: Scheme of the optoelectrical set up for the characterization of photoconductive properties.

used crystal pieces. The deposition rate was 1.6 nm/min for SiO_2 at power of 150 W and pressure of $2 \cdot 10^{-3}$ mbar using a gas mixture of 91%Ar and 9% O_2, and 3 nm/min for SiGe at power of 35 W and pressure of $3.3 \cdot 10^{-3}$ mbar. The sample heating during deposition was performed by clamping the Si substrate between two wires and passing electric current through it, and the temperature was measured using a pyrometer with accuracy that in practice reached ±25 °C in the range 500-900 °C. The deposition was turned on/off using a shutter manually controlled. The sample annealing in this case

was performed in furnace using enriched nitrogen atmosphere. In all cases, electrical aluminum contacts were deposited on the samples using an electron beam evaporator. The structural characterization was performed in an X-ray chamber (PANalytical X'Pert Pro) using XRR and GiXRD methods, and optical and atomic force microscope (AFM). The characterization of the photoconductive properties took place using an optoelectrical set-up, shown in figure 3.2, which consisted on a sample holder with two pin connectors, an electrometer (Kithly 28775), a computer controlled monochromator (SpectraPro 150, 600 grating) and a lamp with known emitting spectrum (ThorLabs OTH10/M). The monochromator scanned over the 300-2300 nm electromagnetic spectrum at 6 sec/nm.

3.2 Experimental strategy

The relationship between processing conditions, sample morphology and photoconductivity was explored through four different experiments, which were designed as follows:

- First of all, the effect of annealing temperature was investigated. Identical samples were grown on silicon substrate by deposition at room temperature, and annealed afterwards at different temperatures.
- Second, the effect that depositing on a hot substrate may have was explored by growing samples at different temperatures on silicon.
- Third, the effect that the substrate may have over the sample growth was explored by growing samples using a different substrate. Borosilicate glass was chosen due to convenience.
- Finally, the internal morphology of the SiGe layer was studied. To that end, the capping layer was not deposited, leaving the SiGe layer exposed to atmosphere and therefore accessible for STM measurements.

3.3 Magnetron sputtering

Sputtering is the ejection of atoms from a surface (**the target**) due to the bombardment of energetic particles [9]. The ejected atoms lose energy as they interact with the surrounding medium until they get deposited again. When this phenomenon is conveniently implemented and optimized for depositing the ejected atoms onto the desired surfaces (i.e. **the substrate**), sputtering becomes a powerful technique for the processing of thin films and coatings. As the sputtering phenomena can be implemented in many different configurations, in practice there are a variety of sputtering methods to choose from. In this project, direct current magnetron sputtering (DC-MS) and radiofrequency magnetron sputtering (RF-MS) where used.

A basic arrangement for the sputtering processing is shown in figure 3.3. For all the three mentioned methods, the setup is placed inside vacuum chambers, into which small amounts of controlled gas mixtures are injected. Even though chemically inert gas species are most commonly used, it is also possible to sputter using reactive mixtures in order to form compounds; a strategy known as **reactive sputtering** [10]. In order to start the sputtering process, a plasma discharge through the gas is first created between the negatively biased target and the grounded metallic sheath around it. The generated ions

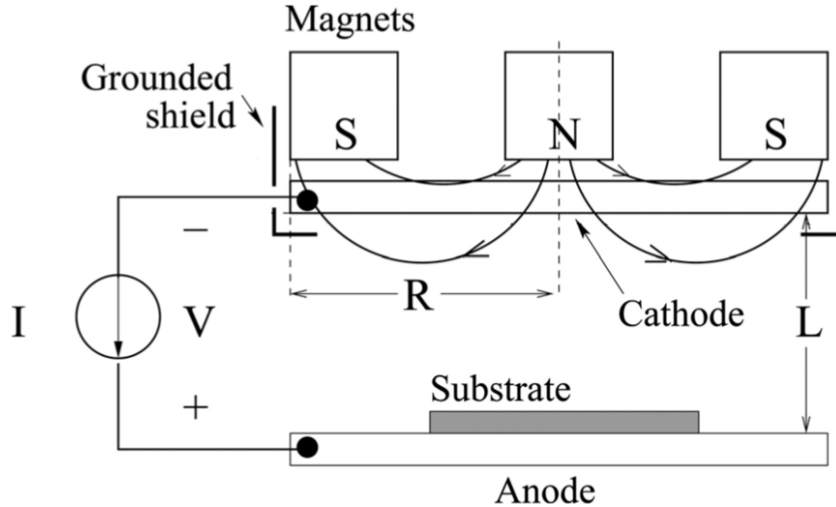

Figure 3.3: Basic setup for magnetron sputtering, extracted from [9]. The set up can be optimized by tuning the distance between the target and the substrate (L), the size of the target R, the characteristics of the power supply (pulsed or continuous bias) and the gas mixture.

are then accelerated towards the target, bombarding its surface and sputtering atoms that will eventually land and deposit on the substrate. During the bombardment, secondary electrons and ions are also generated. The electrons accelerate towards the substrate, ionizing more gas atoms on its way and contributing into the sustainability of the plasma. The secondary ions are accelerated back towards the target, inducing further sputtering. It is known that the quality of the deposited films, as well as the deposition rate, are enhanced by increasing both the plasma density and ion energy [9, 10]. To this end, the plasma is magnetically confined over the target by placing an array of magnets under it, hence the name *magnetron sputtering*.

Direct current magnetron sputtering (DC-MS) is the simplest sputtering method used in this thesis. As the name states, it is powered by a DC power supply that keeps the target in a constant bias. It provides the highest deposition rate among all sputtering methods and can be used both for metallic and semiconductor targets.

Radiofrequency magnetron sputtering (RF-MS) is powered by an RF power supply that continuously inverts the polarization of the biased target at a high frequency (typically ∼MHz). It was developed in order to overcome charge accumulation on poorly conductive targets and, because of it, this technique is able to sputter insulating materials. However, it provides slow deposition rate, and since the resistance of dielectrics change with the applied frequency the impedance of the system must also be taken care of.

For a more detailed insight of the different sputtering methods, the author recommends [9].

3.4 X-ray characterization methods

X-rays are electromagnetic radiation with typical energy values ranging between 100 eV and 100 keV. They are usually produced by the electronic relaxation of atomic K-shells

in high voltage lamps[2], or by the deflection of highly energetic charged particles (as in synchrotron accelerators). Their short wavelength (typically between 10 and 0.01 nm) and their flexible implementation in experimental research convert them into a very powerful tool for the characterization of nanostructures. In many cases, a semiclassical approach[3] is enough to understand the interaction between matter and X-ray, but we shall indistinctly consider the radiation as a wave or a photon as it fits more conveniently in every specific case.

The interaction between X-ray and matter takes place mainly at the atomic electron cloud. This means that the strength of the interaction will be heavily dependent on the electron density of the medium. The cross section σ for a scattering event with an atom changes rapidly with the atomic number Z, following $\sigma \sim Z^4$, and for macroscopic structures the density of the medium will also contribute to the overall interaction. On top of that, when studying crystalline structures, the directionality of the interaction must also be taken into account. The crystal lattice introduces anisotropy, as a propagating wave does not effectively span through the same electronic density in different lattice planes. In the following sections we shall see how this and other properties can be exploited in practice to study chemical composition, sample density and sample structure, including crystallinity and morphology. For a further insight on the fundamentals of light-matter interaction the reader may refer to [7] (especially chapter 7), or to [11, 12] for a more applied reading on X-ray analysis, XRR and GiXRD techniques.

3.4.1 X-ray reflectometry (XRR)

X-ray reflectometry, or XRR, is a powerful technique for the characterization of thin films (below or around 100 nm). It relies on the wave interference phenomenon between several X-ray beams, after the incident beam is reflected and transmitted multiple times through the different sample interfaces, as schematically shown in figure 3.4a. The principle is very similar as the one used in ellipsometry [13] or in X-ray crystallography [11][4]. A sketch of the experimental set-up is shown in figure 3.4b.

---

[2] X-ray lamps also produce a continuous spectrum due to the Bremsstrahlung effect.

[3] In a semiclassical description, one takes into account the quantization of the interacting matter, but describes the radiation as a classical wave.

[4] The angles for constructive interference in X-ray reflectometry are much smaller than in X-ray crystallography. This follows from the fact that the analyzed distances are different in both cases; thin deposited films are always thicker than the spacing between atomic planes in a crystal.

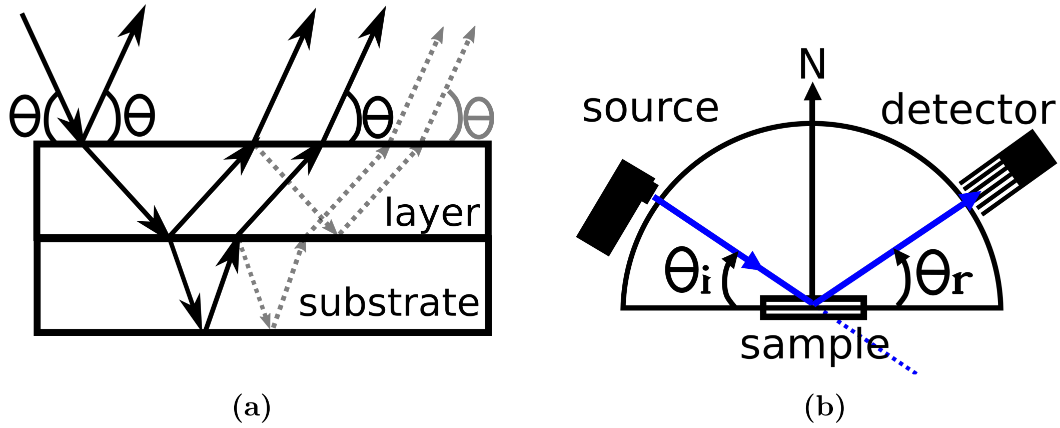

Figure 3.4: **a)** Multiple reflection and transmission through the sample layers. Even though in theory integration through an infinite number of beams have to be considered, in practice only the first order beams are important. **b)** Experimental set-up sketch for XRR, where θ_i must always kept equal to θ_r

In XRR, the source scans the sample over a given angular range while the detector is always kept at the specular angle, that is $\theta_i = \theta_r$. The interference pattern provides information about the optical path inside every layer, which can be used to calculate the sample thickness. While the pattern created by a single ideal layer could in principle be determined analytically, the standard analysis (especially when studying a multilayer arrangement) is performed by fitting the experimental data with computer simulation models. Comparing the deviation between the experimental data and an ideal simulated system, XRR can also provide information about the sample roughness and hints of the chemical composition.

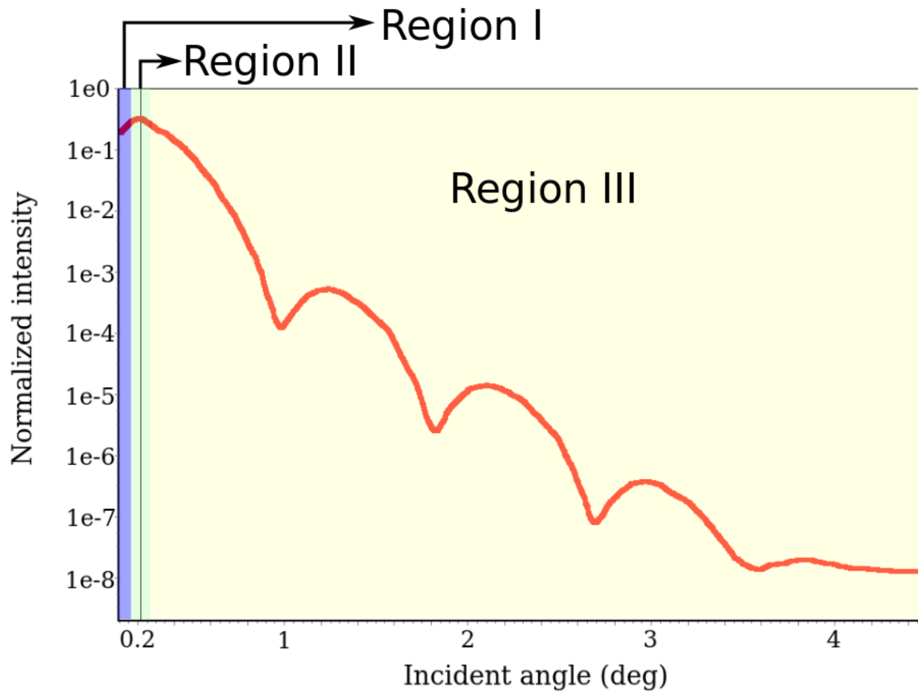

Figure 3.5: Simulated XRR scan of a 5 nm iron layer on a silicon substrate. The line at 0.2 degrees indicate the critical angle.

A typical XRR interference pattern is divided into three well differenciated regions, as can be seen in figure 3.5. The conventional way of presenting XRR data is to plot the measured intensity (in log scale) against the 2θ angle (i.e. twice the angle between the incident beam and the sample surface). For very small angles (region I), the intensity gradually increases as the incident beam starts falling onto the sample surface. Region II is characterized by a more or less constant plateau where almost all of the incident intensity is reflected to the detector, consequence of the total internal reflection phenomena. When the critical angle [11] θ_c is reached (actually $2\theta_c$ as we work in the 2θ frame), the intensity drops several orders of magnitude as the incident beam starts transmitting into the sample layers. It is therefore in region III where the interference phenomena is expected to take place.

Layers with well defined interfaces will produce interference patterns with higher amplitude, while the thickness of the layers will influence the separation between intensity peaks. For a single layer, the interference pattern is expected to show straight forward periodicity with an inverse relationship between sample thickness and pattern period. For a multilayer stack, more complex interference patterns will occur. The roughness of the different interfaces is calculated by comparison of the interference pattern intensity with the diffuse intensity background.

3.4.2 Grazing Incidence X-Ray Diffraction (GiXRD)

The GiXRD is a diffraction technique that exploits the total internal reflection phenomena together with an important and inherent property of X-rays. In contrast to the lower energetic electromagnetic spectrum (including the visible range), the refractive index for X-rays propagating in vacuum or air is higher than of any solid medium[5]. According to Snell's law of refraction, this allows for the total confinement of the X-ray wave outside the sample surface when it is hit from below the critical angle θ_c. However, it is known that the confinement creates an evanescence field that propagates behind the surface. Because of it exponentially decaying nature, the evanescent field is very surface sensitive, and it is an excellent probe for the study of thin layers.

[5] At this point, the reader might feel uncomfortable with the idea that the previous statement violates the principles of special relativity, as $n < 1$ implies higher velocity than the speed of light in vacuum. However, this is a wrong argumentation. Relativity theory prevents anything to have higher **group** velocity than the speed of light in vacuum, but the refraction index refers to the **phase** velocity. Because of it, refraction indexes lower than the unity are not in any conflict with fundamental laws.

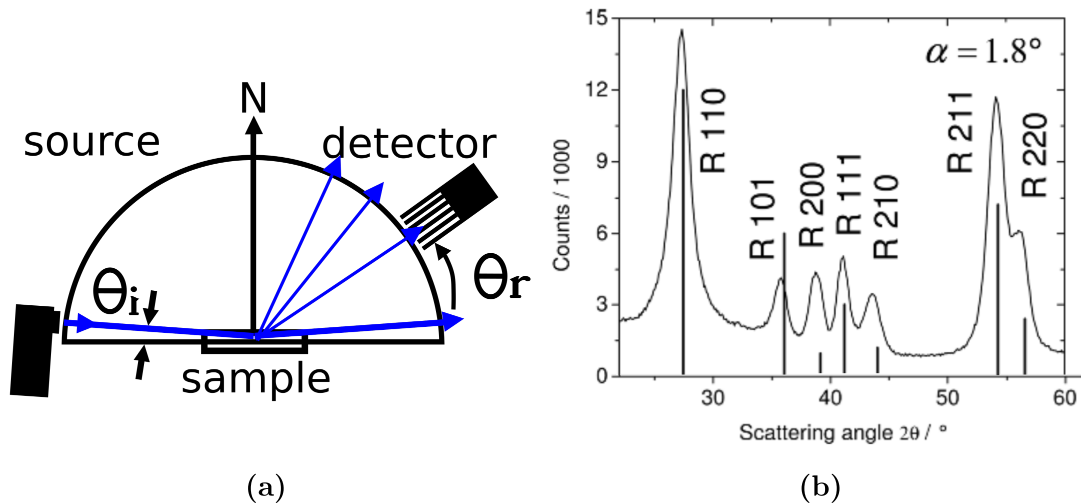

Figure 3.6: a) Set up configuration in GiXRD; the incident angle is kept fixed while the detector scans above the specular angle. **b)** Example of diffraction signal in a GiXRD experiment, where the different Bragg maxima are shown for a rutile Ti crystal. Extracted from [11].

In GiXRD the source is fixed at an angle below θ_c, while the detector scans over the sample to capture the diffracted photons, as shown in figure 3.6a. According to Bragg's law, the evanescent field will scatter in constructive interference at different angles which depend on both the crystalline structure and spacing between atoms in a unit cell (which is in turn dependent to the chemical species involved). A typical example of GiXRD data is shown in figure 3.6b. In practice the registered intensity peaks are usually analyzed in three different ways. First, the angular position of the peaks is compared with a database for the chemical composition and crystalline structure. Second, the peak's width can be used to calculate the average crystallite size [11], expecting thinner peaks for bigger crystallites and ticker peaks for small crystallites. And third, the peak's intensity compared with the background gives a hint about the degree of crystallization.

For the K-Alpha-1 transition (8.05 keV), the main diffractive peaks for policrystalline Si are expected to be at 27.2^o, 46° and 55.8^o, and for polycristalline Ge at 28°, 46° and 54.4^o, in a two theta frame. The reader must note that the most common angle convention for X-ray experiments is different from the one used in optics. In the two theta frame, the angle for the incident beam is measured respect to the surface plane, while the outgoing beam is measured respect the elongation of the incident beam.

Chapter 4

Results and discussion

Sample morphology and crystallization were studied against growth on two different substrates and using different sputtering and annealing conditions. Several identical samples consisting in a trilayer of SiO_2 (100 ± 5 nm, bottom), SiGe (100 ± 5 nm, middle) and SiO_2 (50 ± 2.5 nm, top) were grown at room temperature and on Si substrate. They were annealed in furnace for 5 min at different temperatures, and investigated through XRR and GiXRD.

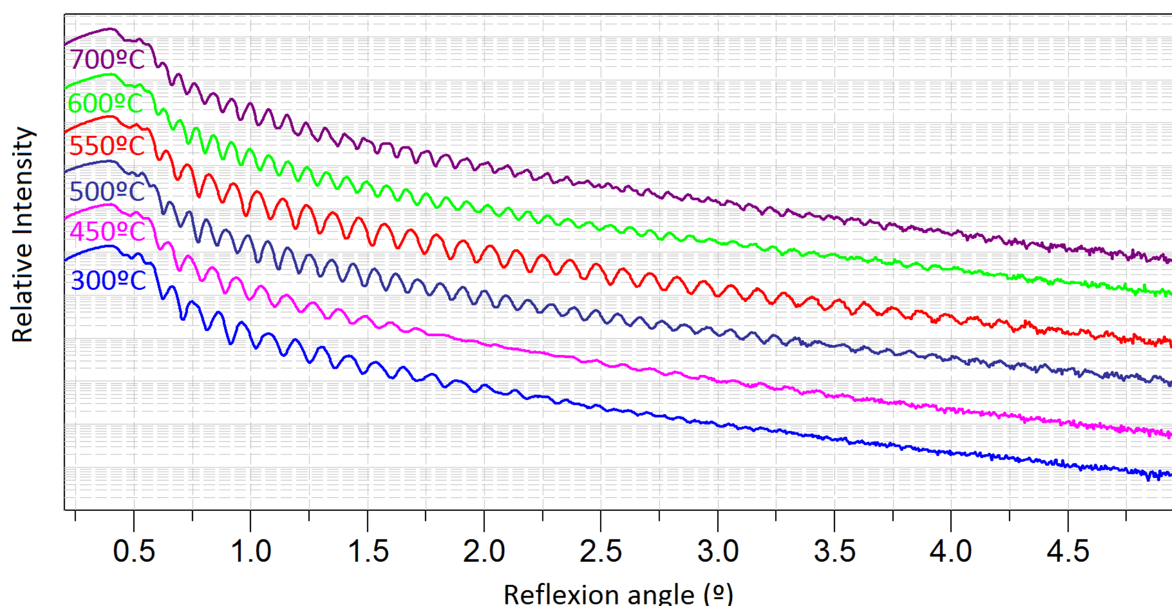

Figure 4.1: Relative reflected intensity against the reflection angle (in a two theta frame) for a layer of SiGe (100 nm) surrounded by two layers of SiO_2, deposited at RT and annealed at different temperatures in furnace.

The reflectivity profile in figure 4.1 shows that the period and the amplitude of the intensity oscillations are approximately the same for all the annealed temperatures. This indicates that the thickness of the deposited layers and the contrast between them is not importantly affected by the annealing process. However, the fact that the oscillations survive different angles before the signal is lost in the background noise suggests that the interlayer roughness is affected. Annealing around 500°C seem to provide the lowest roughness among all measured samples. Besides that, the graph also shows a small angle shift between the different curves for the absolute intensity maximum, found around a

reflection angle of 0.4°. That maximum, located at the critical angle, is where the total reflection phenomenon takes place, and its position is dependent on the sample density[1]. The results show higher critical angles for higher temperatures, suggesting that the density of the films increases with annealing temperature.

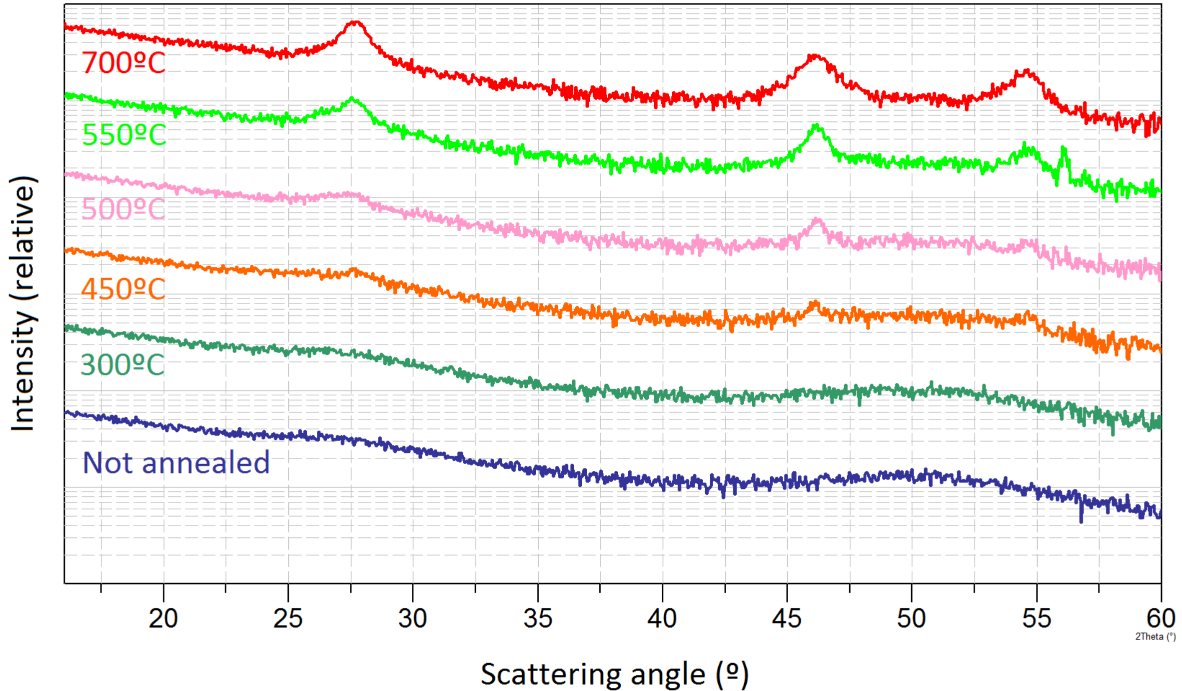

Figure 4.2: Diffracted intensity as a function of angle (in a two theta frame) in a GiXRD measurement for samples deposited at RT on silicon substrate and annealed afterwards.

Figure 4.2 shows the GiXRD measurements of the same annealed samples. The position of the diffracted peaks are in good agreement with the theoretical values stated in chapter 3.4.2. The size of the crystallites were deduced from the mean width of the diffracted peaks, found to range between 5 and 12 nm, for 700 and 500 °C respectively. However, as the theoretical values for Si and Ge peaks are very similar, concentration gradients between both elements[2] in the crystallite must lead to an artifact, and therefore this evaluation method must be taken as a rough lower minimum approximation rather than an accurate measurement. The broad bump that extends from 45° to 60° is characteristic for amorphous SiGe; even though there is not long order arrangement, there is still a range of preferred intermolecular distances, which contribute to the scattering over a broad angle distribution. The decaying background intensity observed from 17.5° to 40° is thought to be a reminiscent influence from the monocrystalline Si substrate.

There is still one more feature worth mentioning in figure 4.2; the sample annealed at 550°C shows a split peak around 55° that is not present in any other case. The position of the splitted peaks are in good agreement with the theoretical values for Si and Ge, showing respectively at 56.1 and 54.6°, and may suggest a phase separation between two elements

[1]Actually, its position is dependent on the refractive index, which happens to be dependent on the density.

[2]Among other factors, this might be produced by difference in the oxidation rate between both elements. Oxygen may penetrate in the layer either by diffusion from the atmosphere or by a non stoichiometric deposition of SiO_x while sputtering.

during the crystallization process. The small difference between the experimental and the tabulated values might arise from the material strain, introduced as thermal stress while cooling in the annealing cycles.

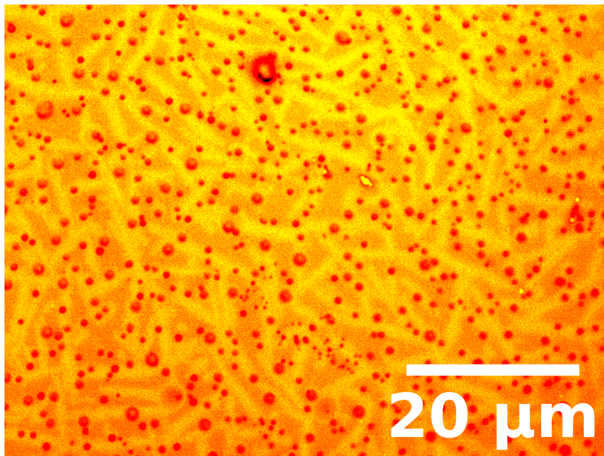

Figure 4.3: Optical image with enhanced contrast of a sample deposited at RT and annealed at 550°C for 5 min.

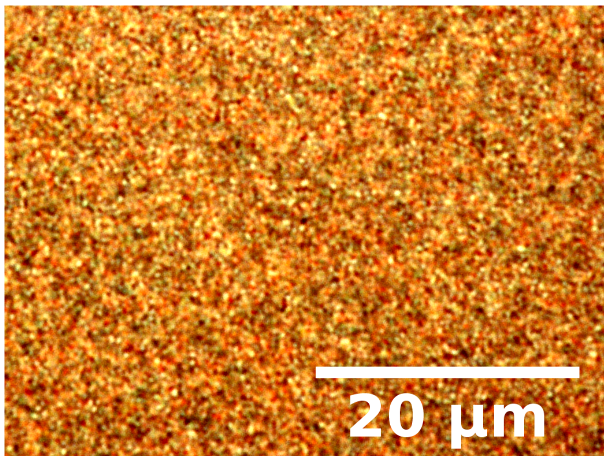

Figure 4.4: Optical image of a SiGe sample deposited at 700°C on a Si substrate

The hypothesis of phases separation was further supported by measurements performed with optical microscope, which show different crystalline domains with sizes ranging between 1 and 10 micrometers approximately, as shown in figure 4.4. The spherical defects that are appreciated in figure 4.4 were further investigated and are thought to be located in the SiO_2 layers, as they could be reproduced in control experiments when depositing this material alone. It was found that both the density and size of the defects are influenced by the deposition conditions, in particular by the external biasing of the sample by charging the sample holder using 20, 40 and 60 V respect the ground potential. However, the presence of defects was not noticed under optical microscope when sputtering on hot substrate or when performing reactive sputtering with a Si target.

When performing optoelectrical measurements, the only samples that revealed photoconductivity were those annealed at 500 and 550°C. Their response against illumination of white light, shown in figure 4.5a, show that the relative number of photogenerated charge carriers is below 2% in both cases. Figure 4.5b shows the behavior of the films when the light source is turned off after being illuminated for a long time (i.e. for several times the recombination time). The relative number of photogenerated charges and their recombination times were calculated as described in section 2.1.2, and they are shown in table 4.1. Overall, these results suggest that the optimal annealing temperature range for the production of functional photoconductive films is less than 250 °C; between 450°C and 700°C. In both cases, the absorption efficiency was too low to perform spectrum dependent measurements with the available optoelectrical equipment.

Table 4.1: Characteristic photoconductive parameters measured at 1 V on SiGe samples sputtered on silicon substrate at RT.

Annealing temperature (°C)	n_{photo}/n_{dark}	τ_r (sec)
500	0.0173	3.893
550	0.0142	4.8216

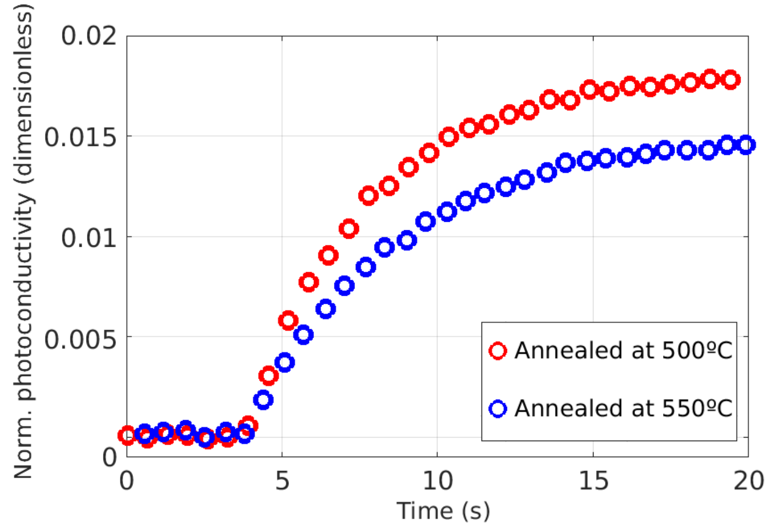

(a)

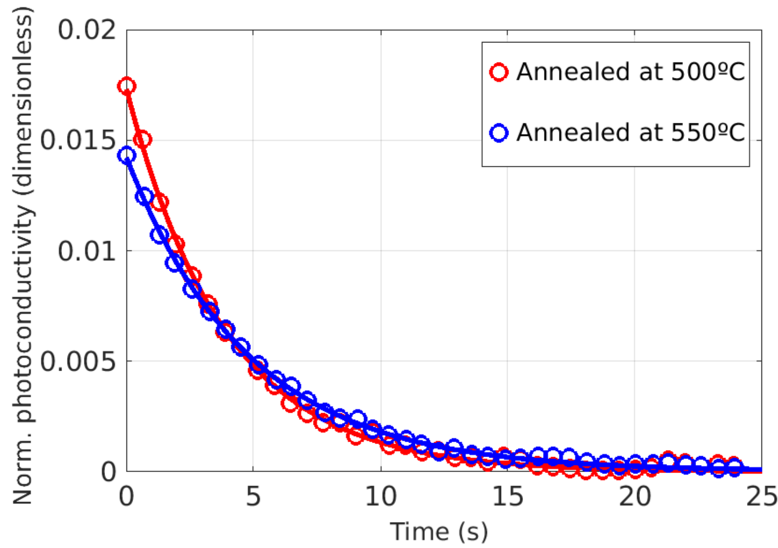

(b)

Figure 4.5: Relative photoconductivity of samples grown at RT and annealed afterwards, for white light illumination turned on (figure **4.5a**) and off (figure **4.5b**). Data fitting using equation 2.14 was performed and the resulting curve is plotted as a solid line in figure 4.5b.

In order to understand the effect that depositing on a hot substrate may have in the crystallization process and how that may affect the photoconductive properties, new

samples with the same layered structure were grown on a heated substrate at different temperatures. The processing was performed using the same methods, but this time the Si substrate was heated by passing electrical current through it. No annealing was performed after the deposition, in contrast as before.

Even though the same layer thickness was attempted, XRR measurements showed a SiGe layer of 75 ± 25 nm, and the fact that the different layer thickness had an effect on the results cannot be ruled out. The GiXRD measurement of those samples are found in figure 4.6, showing thinner and higher peaks in the positions tabulated for SiGe. This fact suggest higher degree of crystallization and bigger crystallite size. Using the width and the position of the diffracted peaks, the crystallites were estimated to have a minimum size of 16 nm. However, later measurements revealed that the crystallites for deposition temperatures of 450°C, 600°C and 700°C were big enough as to be imaged under optical microscope, as may be seen in figure 4.4. For deposition of 300°C, the distance between crystallites was too small to be resolved using optical microscope.

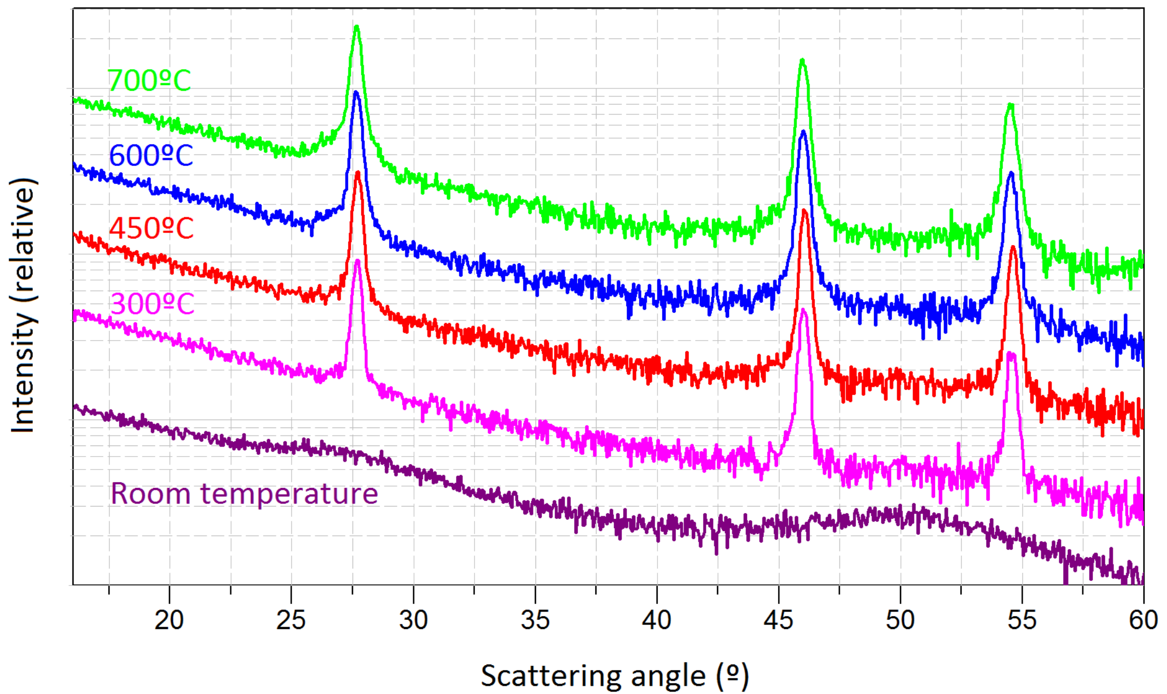

Figure 4.6: Diffracted intensity as a function of angle in a GiXRD measurement for samples deposited at different temperatures on a silicon substrate.

Even though the exact size of the crystallites could not be directly resolved throught the available characterization methods, a higher limit estimation was performed counting the number of crystals per unit area in image 4.4. For deposition temperature of 700°C, 77.5 crystallites were counted inside an area of 39 μm^2, giving an average density of 2 crystals per μm^2. Assuming spherical shape, the radius of the crystals was estimated to be around 400 nm. Using the information provided by GiXRD and optical microscope, the size of the crystallites was estimated to be between 20 and 800 nm in diameter.

Optoelectrical measurements revealed higher relative number of photogenerated charge as compared with the samples that were grown at RT, but in many cases similar recombination times. The reaction of the normalized conductivity upon activation and deactivation of the white light illumination is shown in figures 4.7a and 4.7b, respectively. The

measured photoconductive parameters are shown in table 4.2, being the best efficiency values for the samples grown at 300 and 700 °C.

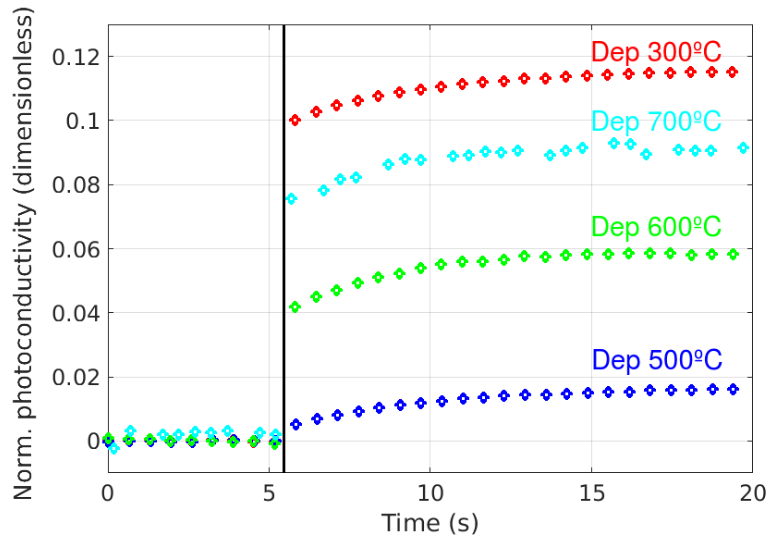

(a)

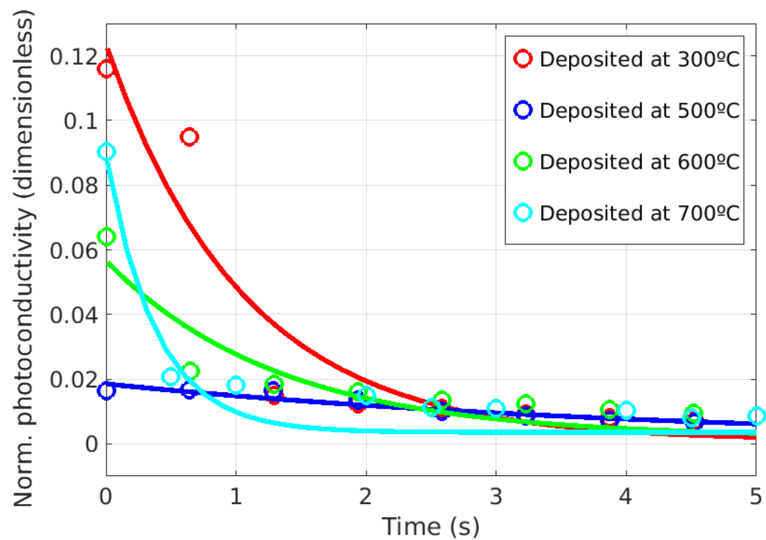

(b)

Figure 4.7: Relative photoconductivity of samples grown on Si substrate heated at different temperatures, for white light illumination turned on (figure **4.7a**) and off (figure **4.7b**). The black and vertical line if figure 4.7a indicates the time when the light source was turned on. Data fitting using equation 2.14 was performed and the resulting curve is plotted as a solid line in figure 4.7b.

The sample deposited at 300°C had efficiency high enough as to perform spectral measurements, showing selective photoconductivity for light illumination with wavelengths between 500 and 1150 nm. The electrical intensity was normalized taking into account the spectrum of the white light source, and the measurements were performed at low bias (0.5 V) in order to avoid strong interference in the band structure. The results are plotted in figure 4.8, and show what could be resonant absorption in the stated wavelength range. This range is not in agreement with the expected resonant energies for transitions

Table 4.2: Characteristic photoconductive parameters measured at 1 V on SiGe samples sputtered on silicon substrate at different temperatures.

Annealing temperature (°C)	n_{photo}/n_{dark}	τ_r (sec)
300	0.123	1.055
500	0.018	4.486
600	0.055	1.324
700	0.086	0.381

between electron-holes ground states (see section 2.2) if the crystallite size measured by GiXRD is to be trusted. However, as previously discussed, the GiXRD measurements for crystallite size are not accurate for SiGe due to the closeness of the diffraction peaks. To the best of our knowledge, the available results are not enough to conclude whether the observed photoconductivity is due to resonance absorption in SiGe quantum dots or just an artifact of the measurement.

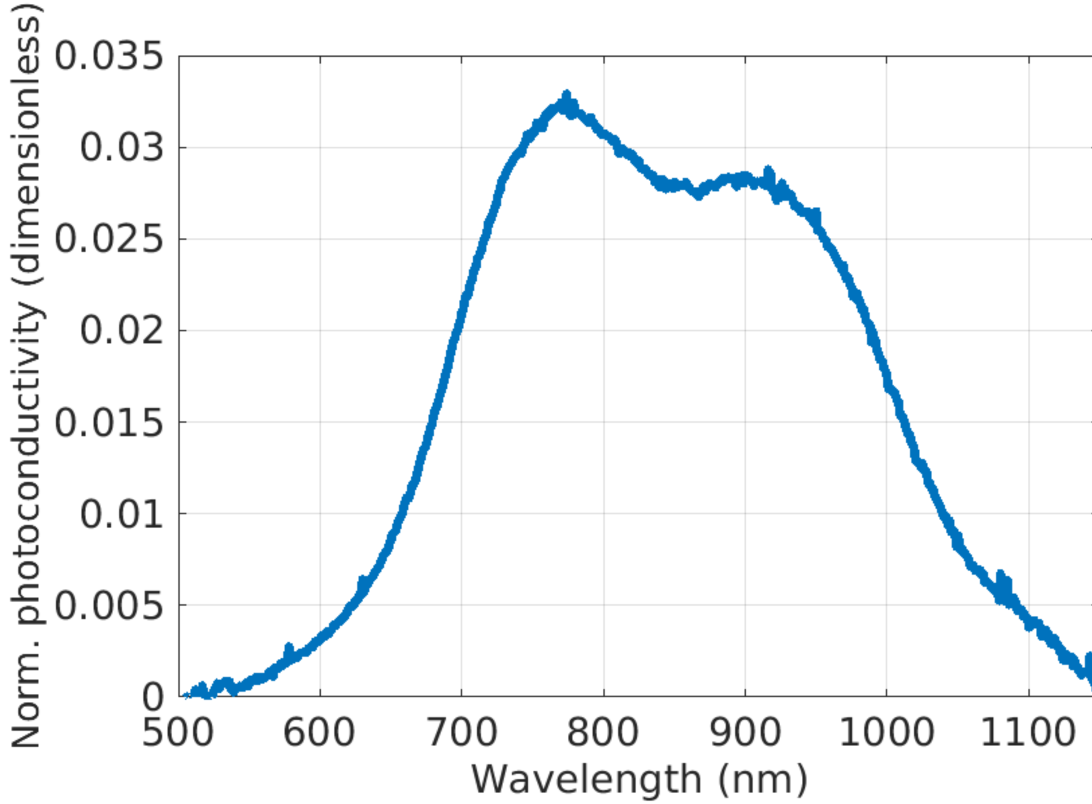

Figure 4.8: Spectral dependence of the normalized photoconductivity in a sample deposited Si substrate at 300°C. The data were normalized using the spectrum of the white light source.

After that, the effect of the substrate was studied. Six samples were grown at room temperature on borosilicate glass substrate, sputtering Ge and Si targets with either neutral or oxidizing gas mixture to deposit Ge, Si and SiO_2, respectively. The intended layered structure was similar as before, but omitting the deposited layer of SiO_2 at the bottom, and with a thicker capping layer of 100 nm SiO_2 at the top (it was 50 nm in

previous samples). The thickness of the SiGe layer was kept at 100 nm. The samples were annealed using RTA at 500ºC, 600ºC and 700 ºC, and measured using XRR and GiXRD. The reflectivity measurements in figure 4.9 show that the roughness of the interphases between layers decreases respect the not annealed sample with increasing temperature, reaching a minimum at 600ºC. However, the definition between layers is completely lost at 700ºC. This could be related to the fact that borosilicate softens near 800 ºC due to its glassy nature. As the material diffusivity increases, molecular mixing between the different layers might take place, creating concentration gradients rather than a steep and well defined interphase.

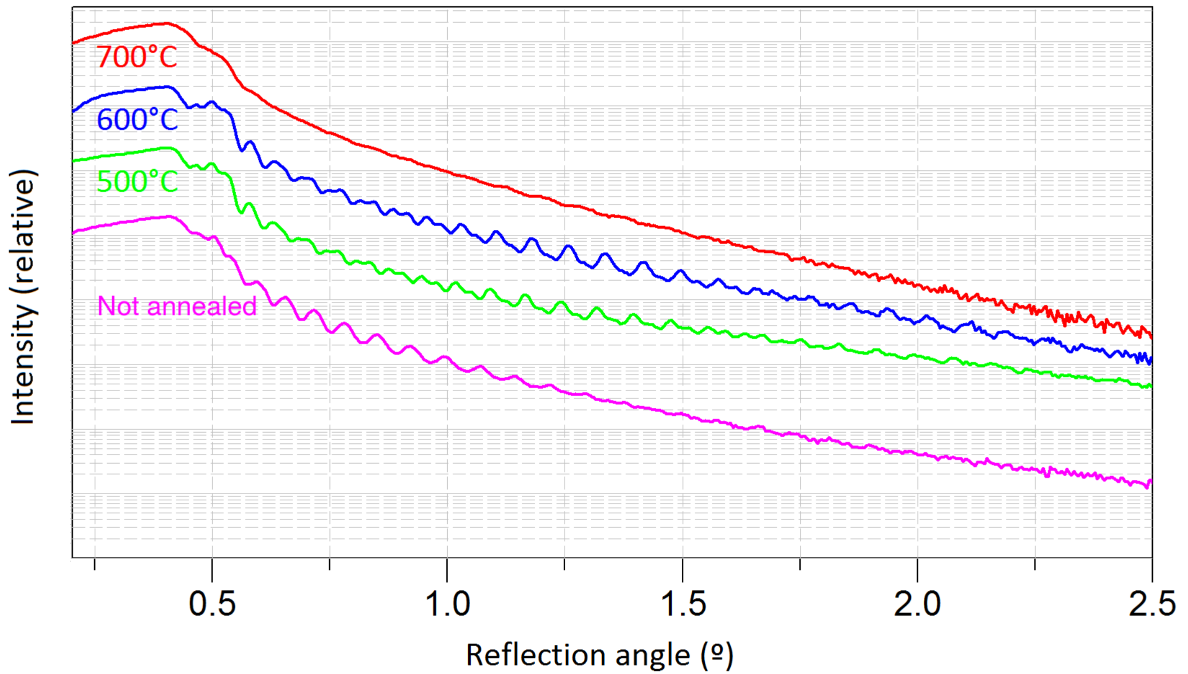

Figure 4.9: Diffracted intensity as a function of angle in a GiXRD measurement for samples deposited at room temperature on a borosilicate glass substrate and annealed afterwards at different temperature.

The GiXRD measurements for the annealed samples did not show any diffractive peaks, neither any other difference compared to the not annealed control. Besides, electrical measurements with voltages up to 20 V found the samples to be completely insulating, with electrical resistances higher than 10^{10} Ω, and no photoconductivity could be measured. The previous facts seem to suggest that the SiGe layer remained amorphous upon annealing, and perhaps became oxidized. This is in clear contrast to the results found for the samples deposited on Si substrate[3], where crystallization was achieved for all annealing temperatures above 450ºC. This might indicate that the layer underneath SiGe (the borosilicate substrate in this case) plays a critical role in the crystallization process. The roughness or the chemical influence of the boron are thought to be the possible key factors.

For completion, growth with deposition on hot borosilicate substrate was performed at different temperatures using the same methods as when deposited at room temperature. However, in order to acces the morphology of the SiGe layer with AFM, deposition of the

[3]Recall that a layer of 100 nm SiO_2 was deposited on every Si substrate before SiGe was sputtered.

top oxide layer was omitted. The reflectivity results in figure 4.10 show that deposition at temperatures between 450°C and 600°C produce very rough films when compared to those deposited at RT and annealed afterwards (figure 4.9). The reason underneath this fact is not well understood, but it is thought to be related with the absence of spatial confinement in the transverse direction (i.e. the absence of the capping layer). As A. Slav et al. discuss in [1], annealing a deposited nanolayer of SiGe without capping layer may result in the formation of nanoislands as the SiGe aggregates around crystallization centers.

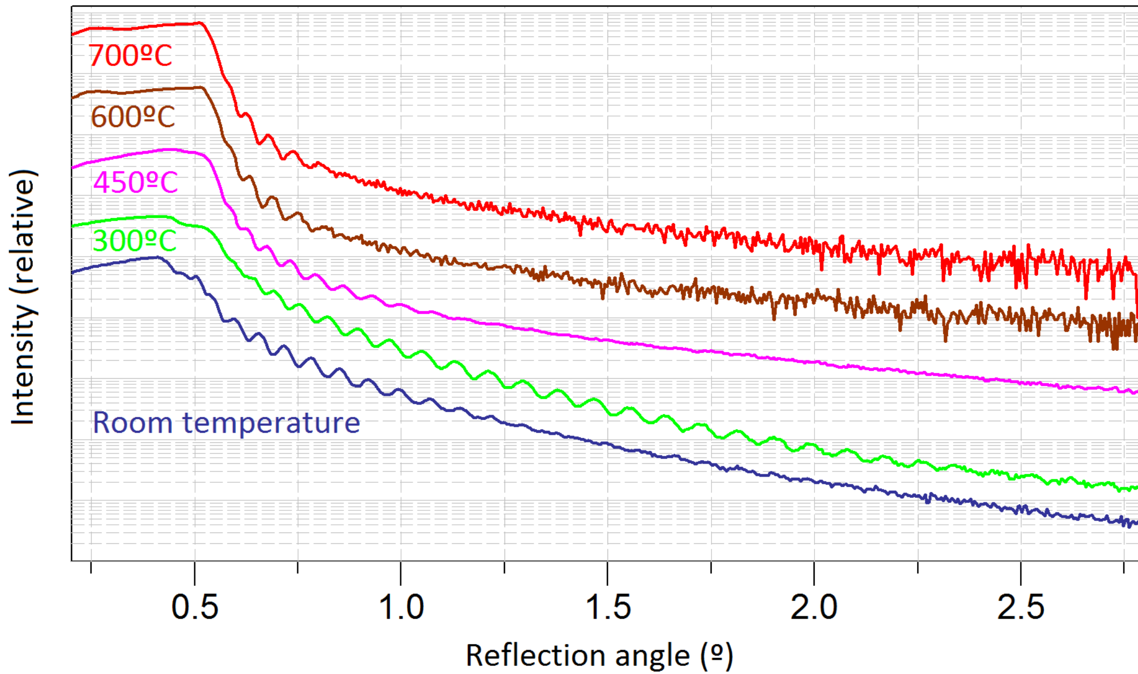

Figure 4.10: Relative reflected X-ray intensity against the reflection angle (in a two theta frame) for layer of SiGe (100 nm) deposited at different temperatures on a borosilicate substrate.

The GiXRD measurements of the same samples, plotted in figure 4.11, showed crystallization taking place between 450°C and 700°C. The sample at 300°C, which presented the lowest roughness in the XRR measurements, seems to be amorphous as no diffraction peaks could be appreciated. This is in contrast with the samples deposited on heated Si substrate, where deposition at 300°C clearly produced crystalline structure. Further comparison between the results in figures 4.6 and 4.11 show higher peaks, and thus higher degree of crystallization, when depositing on hot Si substrate (covered by a grown SiO_2 layer) than when directly depositing on borosilicate substrate at the same temperature. Again, this seems to point to the chemical interaction between the layers as a possible differential factor.

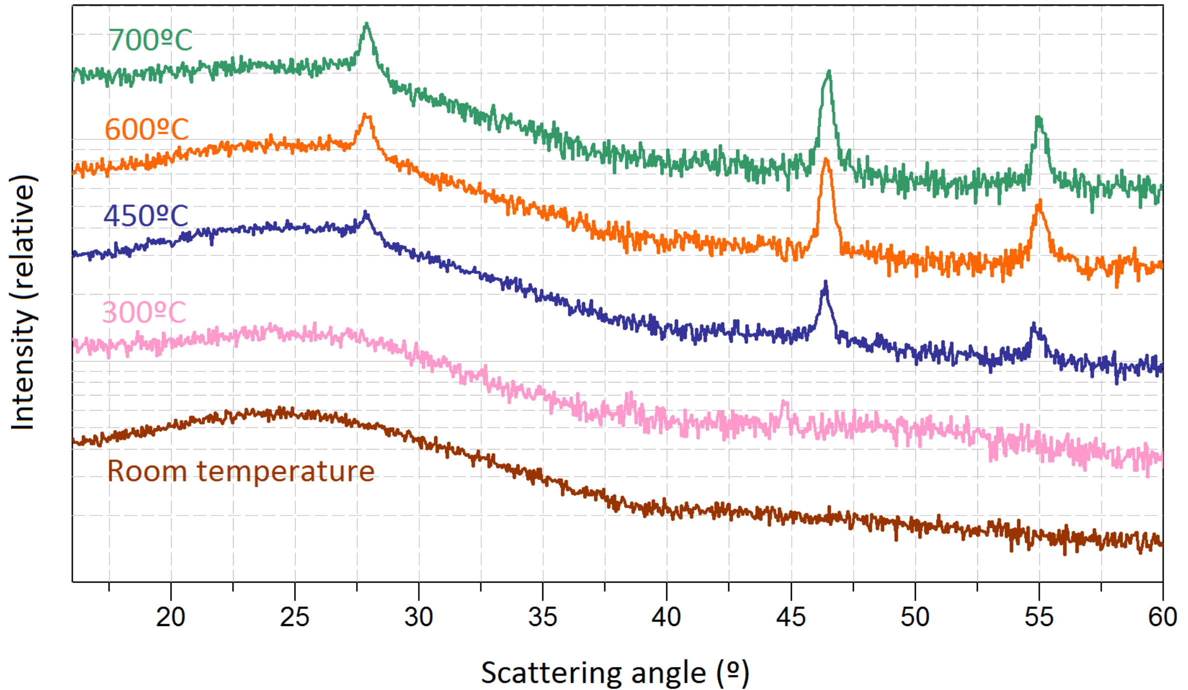

Figure 4.11: Diffracted intensity as a function of angle (in a two theta frame) in GiXRD measurements for samples deposited at different temperatures on borosilicate substrate.

Table 4.3: Characteristic photoconductive parameters measured at 1 V on SiGe samples sputtered on borosilicate substrate at different temperatures.

Annealing temperature (°C)	n_{photo}/n_{dark}	τ_r (sec)
600	0.097	4.398
700	0.065	3.726

Optoelectrical measurements were performed and the results are shown in figure 4.12 and table 4.3. The results reveal absorption efficiencies around 9.7 and 6.5% for the samples deposited at 600°C and 700°C, respectively. The samples deposited at lower temperature did not show measurable photoconductivity. Results in figure 4.12a show a non expected photoconductive behavior; for times between 20 and 40 seconds, the normalized photoconductivity seems to increase linearly. This trend is more accute for the sample deposited at 700°C, and it is also noticeable during the discharge process shown in figure 4.12b, where the normalized photoconductivity for the sample deposited at that temperature seems to decrease with a linear component after $t = 10$ s. The possible introduction of additional terms in the exponential decay stated in equation 2.13 suggests that the generation and recombination of charge carriers might take place through other mechanisms of statistical nature. A recombination process mediated by several impurity levels [14], is proposed as a possible mechanism. The fact that this trend was observed in samples where the capping layer is missing might suggest that the impurities might be located at the SiGe layer surface. However, taking into account that discussed trend is more acute in the sample deposited near the softening temperature of borosilicate glass might suggest that the defects could be created by diffused borosilicate molecules into the

SiGe layer. The absorption efficiency of the samples was not enough to perform spectrum dependent measurements in this case.

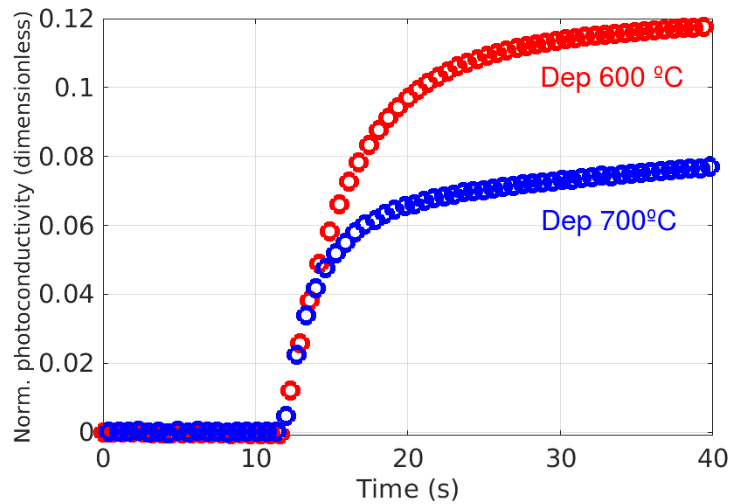

(a)

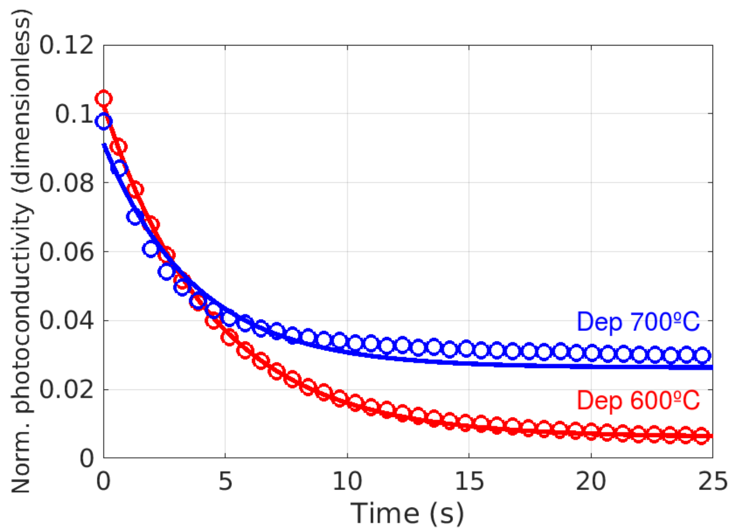

(b)

Figure 4.12: Relative photoconductivity of samples grown on borosilicate substrate heated at different temperatures, for white light illumination turned on (figure **4.12a**) and off (figure **4.12b**). Data fitting using equation 2.14 was performed and the resulting curve is plotted as a solid line in figure 4.12b.

The tendency of SiGe to aggregate around crystallization centers was further investigated by AFM measurements. The aggregation was the most obvious for the sample deposited at 700°C, which showed as the roughest in the XRR measurements (figure 4.10), and its surface profile is showed in figure 4.13. The shown crystalline aggregates have sizes ranging between 50 and 200 nm inside the layer plane, and height ranging between 1 and 20 nm. The sample annealed at 600°C showed a similar aggregation structure, but with broader (400 - 700 nm wide) and shallower (1 - 8 nm height) aggregates. The AFM measurement for the sample annealed at 300°C revealed a very flat surface, with protuberances of only few hundreds of picometers. The aggregation phenomenon is thought to be key in the formation of nanocrystals, and it was further investigated on samples with

different layer thickness. Figure 4.14 shows the AFM picture of a (19 ± 2nm) nm SiGe layer that was deposited under the same conditions as the one showed in figure 4.13. The results show clear evidence that the layer thickness is a determinant parameter in the aggregation phenomenon, showing in this case wider (18 ±4 μm) and higher (40 ± 5 nm) aggregates. The uniformity of the aggregates shape shown by the right inset in figure 4.14 is also remarkable, suggesting that their size might be controlled with high accuracy. The elongated shape of the clusters is thought to be due to the uneven bent of the borosilicate substrate that took place when the sample was cooled after deposition. The fact that the hight of the clusters was as much as the double of the deposited layer suggests that the aggregation might have left parts of the substrate uncovered by SiGe, which is critical for the formation of well defined and separated nanocrystals.

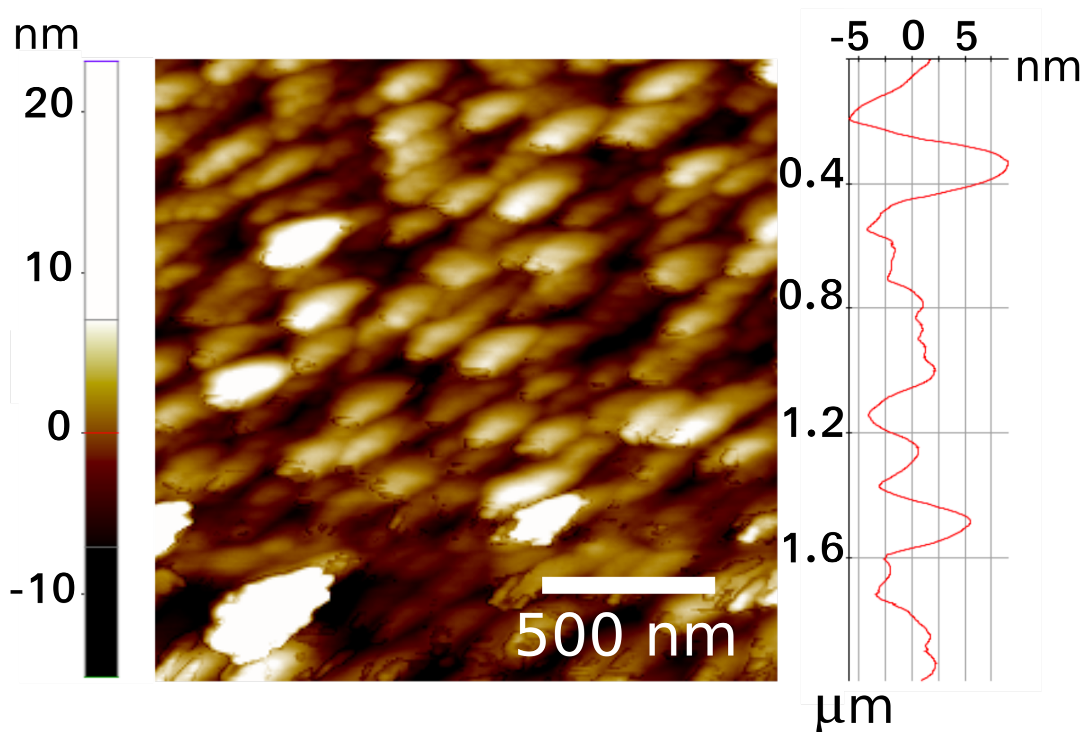

Figure 4.13: AFM image of the surface of a SiGe layer (100 ± 5 nm) deposited at 700°C on borosilicate substrate. The right inset corresponds to a horizontal sectional profile located in the middle of the image.

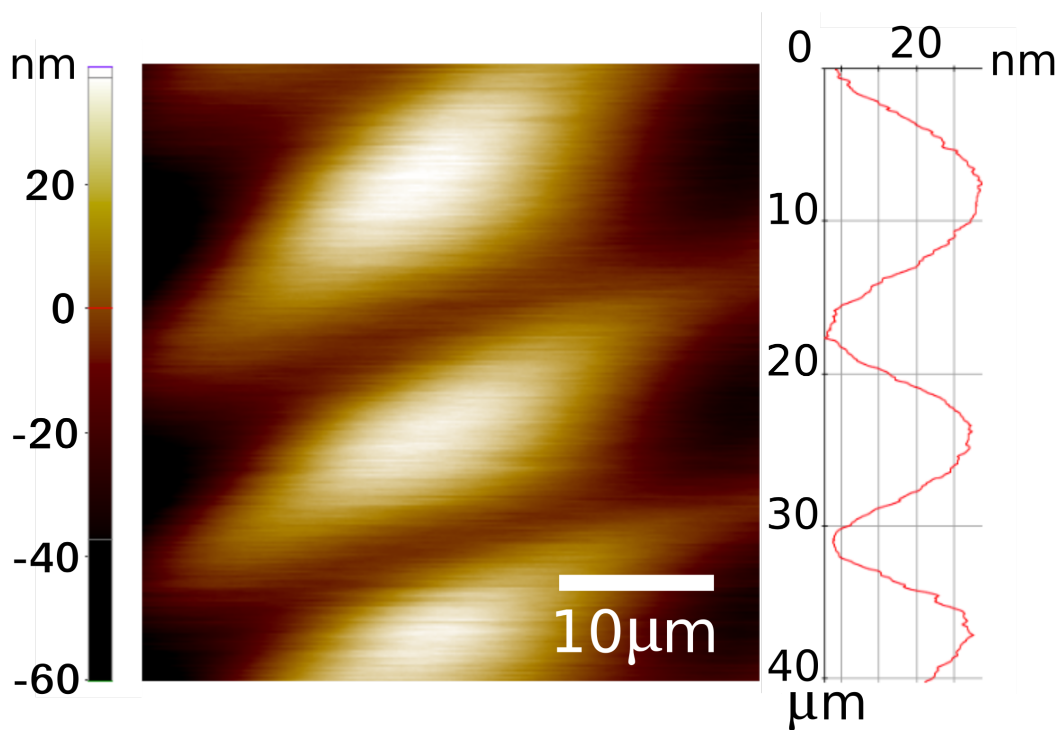

Figure 4.14: AFM image of the surface of a SiGe layer (19±2nm) deposited at 700°C on borosilicate substrate. The right inset corresponds to the sectional profile perpendicular to the elongated aggregates.

Chapter 5

Outlook

In this thesis, the processing of thin SiO_2 layers (thickness $\leq$ 100 nm) functionalized with SiGe nanoparticles for highly selective photoconductivity was studied. Different layers of SiO_2 and SiGe were deposited using DC and RF magnetron sputtering, and their structural and photoconductive behavior characterized. The sample processing was performed against different annealing and deposition temperatures, and using two different substrates: monocrystalline Si (001) and borosilicate glass. The results clearly showed higher crystallized structure when depositing on hot substrate, with bigger crystallite size for increasing temperatures. Depositing at room temperature and annealing afterwards happened to produce smoother films with better defined interphases, but more prone to remain amorphous. Using monocrystalline Si (001) as substrate seemed to be advantageous for sample crystallization in comparison to borosilicate glass. The reasons behind this fact are not well understood, but the different substrate roughness and chemical interaction are suggested as possible influential factors.

Optoelectrical measurements seemed to show that films with crystalline structure show better photoconductive properties. However, the results were not conclusive about the relation between sample roughness and photoconductivity. One sample with selective photoconductivity was achieved using deposition on hot Si substrate (300°C), showing maximum sensitivity for light of 780 nm in wavelength. However, whether the absorption selectivity is due to resonant absorption in SiGe nanocrystals or to an artifact in the characterization measurements due to a wrong calibration of the white light source is not clear. Further investigation with more advanced optoelectrical setup and transmission electron microscope (TEM) to directly determine the internal structure of the samples could be beneficial in order to better understand the relation between sample morphology and photoconductivity.

The aggregation of SiGe in nanoislands was observed and investigated. The role of nanoislands formation is though to be key for the processing of selective photoconductive films, as they might be precursors of the nanocrystals formation. If that was the case, higher layer roughness would be preferred, as it indicates a sharper aggregation. It was found that the aggregation phenomenon in SiGe films with thickness of 19 nm was more prominent than in films with thickness of 100 nm, suggesting that thinner films are preferred for the formation of nanoislands. However, as the film thickness decreased the aggregated clusters seemed to become wider. Further investigation on the aggregation effect in nanoislands is thought to be key in achieving a controlled processing of SiGe nanocrystals, and therefore further pursuing this experimental line is highly auspicated.

Bibliography

[1] A. S. et al., "Influence of preparation conditions on structure and photosensing properties of GeSi/TiO2 multilayers," in *IEEE International Semiconductor Conference - CAS*, 2017.

[2] J. H. Davies, *The physics of low-dimensional semiconductors; an introduction.* 2005.

[3] C. P. et al., "Transport mechanisms in SiO2 films with embedded germanium nanoparticles," in *Proceedings of the International Semiconductor Conference, CAS*, 2012.

[4] F. L. et al., "Photoconductive gain of SiGe/Si quantum well photodetectors," *Optical materials*, vol. 27, pp. 864–867, 2005.

[5] M. C. T. Bahaa E. A. Saleh, *Fundamentals of photonics.* 1991.

[6] J.R.Hook and H.E.Hall, *Solid State Physics.* 1991.

[7] C. J. Foot, *Atomic Physics.* 2005.

[8] V. Trivedi, "Evaluation of rapid thermal processing systems and their role in fabrication of next generation core CMOS fabrication," Master's thesis, University of Florida, 2001.

[9] J. T. G. et al., "High power impulse magnetron sputtering discharge," *Journal of Vacuum Science and Technology*, vol. 30, 2012.

[10] J. G. et al., "Reactive high power impulse magnetron sputtering," *The Twelfth International Symposium on Sputtering and Plasma Processes*, pp. 194 – 196, 2013.

[11] M. Birkholz, *Thin film analysis by X-ray scattering.* 2006.

[12] J. Als-Nielsen, *Elements of Modern X-ray physics.* 2008.

[13] J. J. J. B. Tobias Holmgaard, Niels Anker Kortbek, "Ellipsometry," Master's thesis, Aalborg University, 2004.

[14] A. Hangleiter, "Nonradiative recombination via deep impurity levels in silicon: Experiment," *Physical review B*, vol. 35, no. 17, 1987.